Journal of Electronics and Electrical Engineering
https://ojs.wiserpub.com/index.php/JEEE/

Research Article

Enhanced Harmonic Suppression for a Miniaturized Hairpin-Line Bandpass Filter with Meander Spurline

Tarun Kumar Das[1*], Sayan Chatterjee[2]

[1] Electronics and Communications Engineering Department, Future Institute of Engineering and Management, Kolkata, India
[2] Electronics and Telecommunication Engineering Department, Jadavpur University, Kolkata, India
E-mail: tarunj1979@gmail.com

Received: 18 February 2024; **Revised:** 6 May 2024; **Accepted:** 3 June 2024

Abstract: The design of a fourth-order centrally corrugated double-folded hairpin line bandpass filter with a broad stopband and enhanced selectivity is demonstrated in this article. Initially, a double-folded hairpin-line bandpass filter (DFHLBF) is designed from a fourth-order conventional hairpin-line bandpass filter (CHLBF), which is centred at 2.5 GHz and has a fractional bandwidth of 3%. This results in a 68% size reduction. With this folding mechanism, the filter's skirt characteristic is only enhanced at the upper passband edge, resulting in an attenuation level of 40 dB at 2.65 GHz. The capacitive loading has then been incorporated by periodic rectangular corrugations that have disturbed the folded arms. Because of the high capacitive coupling between the folded arms, a symmetrical passband with an attenuation level better than 40 dB at both edges has been observed. Besides, a size reduction of 14% than that for the DFHLBF has been achieved. However, because of the imbalance of the modal phase velocities in the inhomogeneous microstrip filter construction, the stopband's attenuation level climbs to 8 dB. Rectangular meander spurlines have been added between the connected arms of the neighbouring centrally corrugated cells of the filters as a way to lower the attenuation levels of the harmonics. This creates a slow-wave effect between the odd- and even-modes of the propagating signals. This results in an overall size reduction of 81% over the standard hairpin-line filter and an enlarged stopband of up to $4.36f_0$ with a rejection level of 42 dB.

Keywords: bandpass filter, hairpin-line, corrugations, spurline, wide stopband

1. Introduction

The internationally distributed Internet of Things (IoT) system is driving an increase in demand for 5G wireless communication systems with expanded functionality [1]. In order to address these demands, small, highly selective hairpin line filters have grown in favour [2, 3, 4]. Additionally, tunable hairpin line filters using variable capacitances and resistive terminations have been proposed in [5]. However, their uses are restricted in the miniature receivers due to their large sizes ($0.31\lambda_g \times 0.24\lambda_g$). Several types of research have been conducted in this regard to develop small bandpass filters with improved passband performances, including the use of multi-folded stepped-impedance resonators (SIR) [6, 7], capacitively coupled stub-loaded stepped-impedance resonators (SRR) [8], stair-case hairpin lines [9], folded hairpin lines resembling helicopters [10], and three-dimensional integrated through-silicon via (TSV) technology [11]. In this regard, a cascading bandstop filter with resistive termination has been presented in [12] as a two-port reflectionless bandpass filter, where out-of-band energy was absorbed using the resistive part of the bandstop filter section, leading to enhanced stopband

DOI: https://doi.org/10.37256/jeee.3220244469

reflectionless properties. However, the filter's size and bandwidth are relatively large, which limit its use in contemporary miniaturized 5G wireless systems. Nevertheless, [5, 6, 7, 8, 9, 10, 11, 12] does not address the effects of such compactness on the harmonic attenuation levels.

Harmonics create severe problems in mixers and frequency synthesizers used in wireless communication systems. Besides, harmonic signals can obstruct other broadcasting or communications protocols, distilling intermodulation [13]. To attain harmonic suppression, two main methods have been explored: (1) harmonic suppression for traditional hairpin line filters [14, 15] and (2) harmonic suppression for compact, folded hairpin line filters [16, 17, 18] by the use of diverse nonuniform perturbations. These disturbances are primarily used to lessen the disparity between the odd- and even-mode phase velocities of the EM waves travelling in the linked regions between the lines. Most designs show a slow-wave influence in the odd-mode due to nonuniform disturbances, while the even-mode is usually untouched. Thus far, several techniques have been investigated: the Wiggly-line [14], quasi-Minkowski fractals [15], stepped impedance resonators [17], open-ended stepped-impedance stubs [16], and stub-loaded resonators [18]. The rejection bandwidth is constrained to $3f_0$, while the rejection intensity is limited to 30 dB only. The filter sizes in [14, 15, 16, 17, 18] are still rather large, though.

In order to achieve more size reduction and harmonic suppression, researchers incorporated spurlines [19, 20, 21] by utilizing their bandstop resonance. A high-temperature superconducting bandpass filter with slotted SIRs was reported to have a large stopband in [21], with a rejection level of 22 dB up to $5.64f_0$. For the fourth-order double-folded hairpin line bandpass filters (DFHLBF), the utilisation of a conventional L-shaped spurline (stopband rejection level of 38 dB up to $4.48f_0$) has recently been thoroughly investigated in [22]. A modified T-shaped spurline (stopband rejection level of 39 dB up to $3.2f_0$) [23] and a meander spurline (stopband rejection level of 40 dB up to $4f_0$) [24] were used in [23, 24] to demonstrate similar efforts. In order to accomplish a size decrease of more than 20%, the centre folded arms of [22, 23, 24] have been enlarged upon in [25] by using trapezoidal-shaped corrugated arms in their place. Incorporating trapezoidal-shaped meander spurlines has therefore led to a rejection level of 35 dB up to $3.88f_0$. Subsequently, a compact differential dual-band wide-bandpass filter (size of $0.31\lambda_g \times 0.35\lambda_g$) has been proposed in [26], in which doubly-coupled U-shaped structures have been connected through a defected Sierpinski fractal-based low impedance transmission line. As a result, an upper stopband rejection bandwidth of $3.28f_{01}$ (f_{01} is the center frequency of the first passband) with a rejection level of 30 dB has been obtained. Very recently, as an alternative technology, an all-metal wideband (31%) frequency-selective surface bandpass filter for TE and TM polarizations has been proposed in [27]. The proposed filter, being completely passive without any dielectric substrate, is mechanically robust, less weighty, optically transparent, and has wide upper and lower stopbands with sharp skirt characteristics. Subsequently, in [28], single radial stubs have been exploited in conventional hairpin-line filter structures to achieve a wide upper stopband rejection bandwidth up to $10f_0$ with a rejection level of 32 dB. However, the size of the filter is quite large ($0.64\lambda_g \times 0.43\lambda_g$) restricting its applications where circuit area is limited.

The study of [25] has been further investigated in the current work in order to produce a more transportable double-folded hairpin line bandpass filter and provide greater harmonic suppression with a broader stopband. Trapezoidal corrugations have replaced rectangular corrugations in the centre folded arms of the hairpin lines of [25], resulting in a size reduction of more than 16% over [25]. The rectangular meander spurline has subsequently been used to disturb the connected arms of the folded cells of the filters in order to achieve modal phase velocity correction. Consequently, by adding abrupt transmission zeros at the passband edges with an attenuation level of greater than 75 dB, the skirt selectivity of the filter has been improved. Furthermore, the bandstop characteristics of spurlines might result in the formation of several gearbox zeros in the stopband. Ultimately, the measurement yielded an expanded stopband with a rejection level of 42 dB up to $4.36f_0$, and both the stopband rejection level (20%) and stopband bandwidth (12.4%) improved over [25]. Up to 81% less space is obtained in the optimised filter's dimensions than in the classic filter [22, 23, 24]. The properties of the substrate material used in this investigation are as follows: thickness $h = 1.6$ mm; dielectric constant $\varepsilon_r = 4.4$; and loss tangent $\tan\delta = 0.02$. The Zeland IE3D EM wave simulator has been used for all simulation-based research.

2. Corrugated double-folded hairpin line cell

For the resonance frequency of f_0 = 2.5 GHz, Figure 1 shows the conversion of the unit conventional hairpin line (CHL) cell to the double-folded hairpin line cell (DFHL) and then to the centrally corrugated double-folded hairpin line (CCDFHL) cell. The DFHL cell has a circuit area of 44.84 mm^2, the CHL cell has 69.48 mm^2, and the CCDFHL cell has 39.3 mm^2. The uniform resonator has a width of 1 mm. As a result, the CCDFHL cells had a 43.4% size reduction over the CHL cell. The uniform connection gaps between portions are set at 0.2 mm for simplicity's sake. Figure 2a compares the three cells' wideband resonant properties, which are visible from $|S_{21}|$ (dB). Figure 2a shows that the CCDFHL cell's attenuation level at f_0 = 2.5 GHz has steadily dropped to a minimum (25 dB) as a result of the two side arms' reduced effective conductive area as a result of inward folding. In addition, the CCDFHL cell's $2f_0$ and $3f_0$ positions have moved to lower frequency areas, and the related attenuation levels have decreased. The decrease in the total effective electrical length is the cause of this. The symmetry line T-T′ in Figure 1 for the CCDFHL cell indicates an important finding: the additional capacitive coupling effects in the inner coupling zones between the corrugated folding arms can cause a gradual reduction in the bandwidth at f_0. The comparison of the $|S_{21}|$ (dB) curves at f_0 and $2f_0$ between the CCDFHL cell with trapezoidal [25] and rectangular corrugations has been explored in Figure 2b,c respectively. It has been observed from Figure 2b that for the CCDFHL cell with rectangular corrugations, the center frequency (f_0) has been shifted to 2.47 GHz from 3.15 GHz for trapezoidal corrugations [25]. This is due to the increment in the overall electrical length of the central resonator with rectangular corrugations having sharp bent edges over trapezoidal corrugations [25].

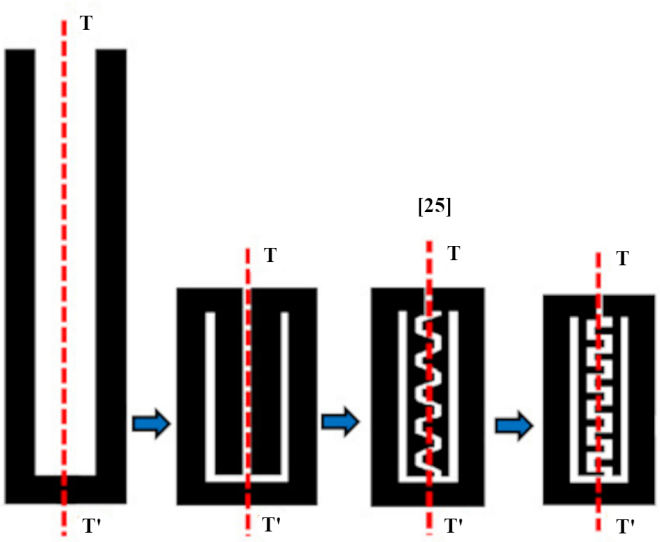

Figure 1. Folding mechanism that converts the trapezoidal to rectangular form of the conventional hairpin line (CHL) cell into the DFHL and CCDFHL cells in turn. The line of symmetry is T-T'.

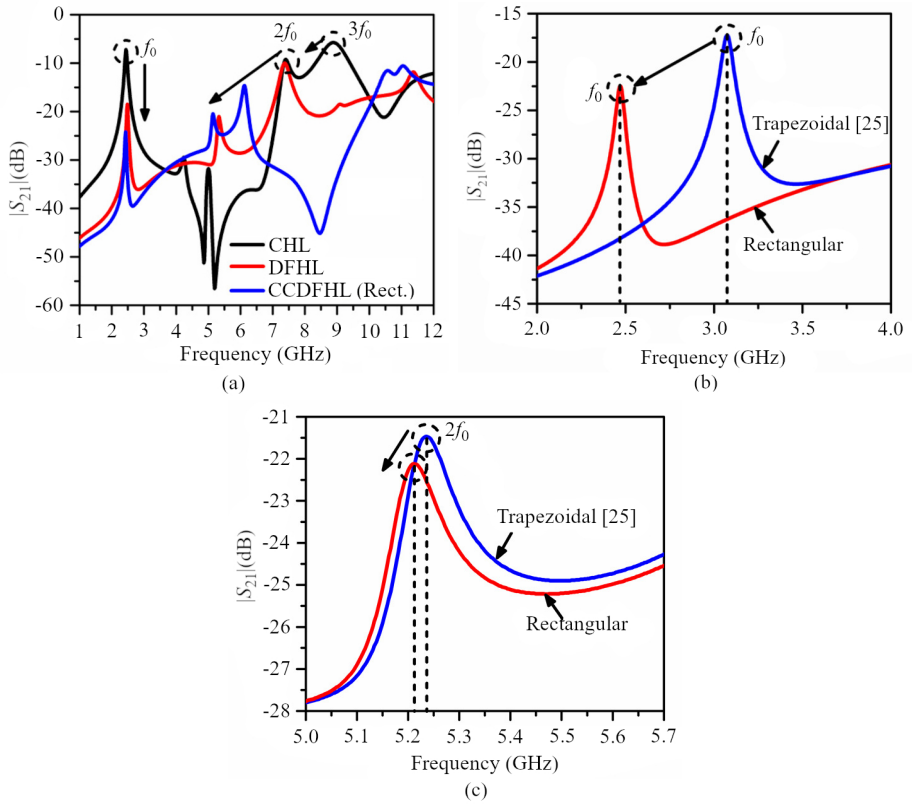

Figure 2. (**a**) Comparison of $|S_{21}|$ (dB) of the rectangular shaped CCDFHL cell with the CHL and DFHL cells, (**b**) comparison of $|S_{21}|$ (dB) for the center frequency (f_0), and (**c**) the second harmonic frequency ($2f_0$) between the proposed rectangular shaped and trapezoidal shaped CCDFHL cells [25].

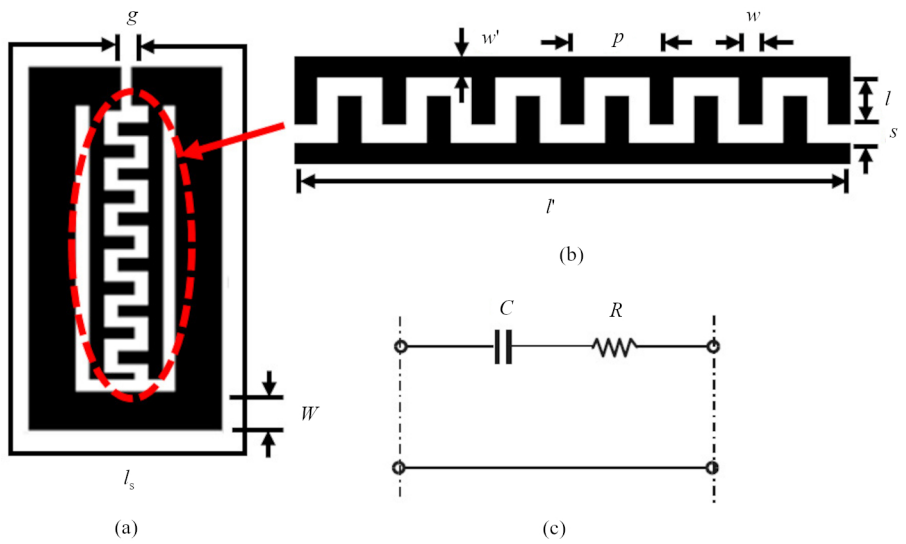

Figure 3. (**a**) Layout of the unit CCDFHL cell, (**b**) structure of an interdigital capacitor (IDC), and (**c**) ideal equivalent circuit diagram of the IDC in lumped elements.

In addition, the attenuation level at f_0 has been decremented from −17 dB to −23 dB (relative decrement of 26%) for the proposed rectangular shaped cell compared to that with trapezoidal corrugations [25] due to the multiple capacitive coupling between the corrugations. By optimal tuning of the dimensions and periodicity of the rectangular corrugations,

the insertion loss at f_0 can be reduced. Moreover, it has been observed from Figure 2c that the attenuation level at $2f_0$ has been reduced for rectangular corrugations-based CCDFHL cell over trapezoidal corrugated CCDFHL cell. It signifies the better harmonic suppression ability of the rectangular corrugations-based CCDFHL cell. Thus, Figure 2b,c justify the effectiveness of the proposed rectangular CCDFHL over trapezoidal CCDFHL. Figure 3a shows the arrangement of the unit CCDFHL cell with various dimensions. An interdigital capacitor (IDC) with an overall length of l' and a transmission line with length l_s and width W are combined to form the structure. The cell's two folded arms are separated by g. Figure 3b highlights the structure of the central IDC, and Figure 3c depicts its ideal equivalent circuit in lumped elements. For the sake of simplicity, Figure 3c ignores the effects of the electric field while taking into account those of the magnetic field between the fingers (inductive coupling). The coupling between the slots is represented by the value C, while the conductive portions of the slots are represented by the resistance R. An additional inductance would be added in series with R and C if magnetic effects are to be considered. Equation (1) provides an approximation for the interdigital capacitance C [29].

$$C = (\varepsilon_r + 1)\, l\, [(N-3)A_1 + A_2]\,(\text{pF}) \tag{1}$$

$$A_1 = 4.409 \tanh\left[0.55\left(\frac{h}{w}\right)^{0.45}\right] \times 10^{-3}\ (\text{pF/mm}) \tag{2a}$$

$$A_2 = 9.92 \tanh\left[0.52\left(\frac{h}{w}\right)^{0.5}\right] \times 10^{-3}\ (\text{pF/mm}) \tag{2b}$$

Equation (1) takes N as the number of fingers, l and w as the length and breadth of each finger, respectively, and C as the capacitance per unit length along l'. It also takes into account the capacitances per unit length of the two outside fingers, A_1 and A_2. Moreover, ε_r is the substrate material's relative dielectric constant, and h is the substrate material's thickness in millimetres. For the sake of simplicity, the coupling gap between the fingers is taken to be constant across the whole structure. Equation (3) provides the interdigital capacitor's series resistance as

$$R = \frac{4}{3}\frac{l}{wN}R_s \tag{3}$$

where R_s is the conductor's sheet resistance in ohms per square for the capacitors. The Q-factor of the IDC is given by Equation (4) as

$$Q_c = \frac{1}{\omega C R} \tag{4}$$

For the unit CCDFHL cell, as shown in Figure 3a, with the resonant frequency at 2.5 GHz, the dimensions have been estimated as l_s = 26.82 mm, g = 0.3 mm, and W = 1 mm; while the dimensions have been chosen as l' = 5 mm, $w = w'$ = 0.2 mm, s = 0.2 mm, l = 0.4 mm, and p = 0.8 mm for the IDC. By using such dimensions, the values of C, R and Q can be calculated for the IDC from Equations (1), (3), and (4) as C = 0.1036 pF, R = 0.1023 mΩ, and $Q = 6.0043 \times 10^6$. Figure 4 displays the analogous circuit diagram for the CCDFHL. Using traditional transmission line theory, the values of the lumped elements may be computed. The values of the lumped elements have been calculated as L_1 = 2.424 nH, L_2 = 2.991 nH, L_3 = 1.697 nH, C_{p1} = 0.454 pF, C_{p2}= 0.364 pF, C_{p3} = 0.089 pF, $C_{g1} = C_{g2} = C_{g3}$ = 0.015 pF, C = 0.1036 pF, and R = 0.1023 mΩ. Figure 5a compares the simulated $|S_{21}|$ (dB) for the unit DFHL [22] and CCDFHL cells. It has been revealed that the CCDFHL cell has generated a symmetric and narrow passband, as compared to the DFHL cell [22]. On the other hand, the additional capacitance and slow-wave effects of the central IDC cause the attenuation level at f_0 = 2.5 GHz to drop for the CCDFHL. Such comparison justifies the effectiveness of the CCDFHL cells over the DFHL cells [23] as the former can be used to design a more compact narrow-band filter. It is also observed from the distribution of surface currents, with reference to Figure 5b, that maximum currents propagate through the side arms; however, less amount of currents concentrate in the central IDC due to the slow-wave effect. Hence, it can be

concluded that maximum amount of signal would be coupled to the adjacent arms of the next cell, enabling the design of the higher-order filters in the next section.

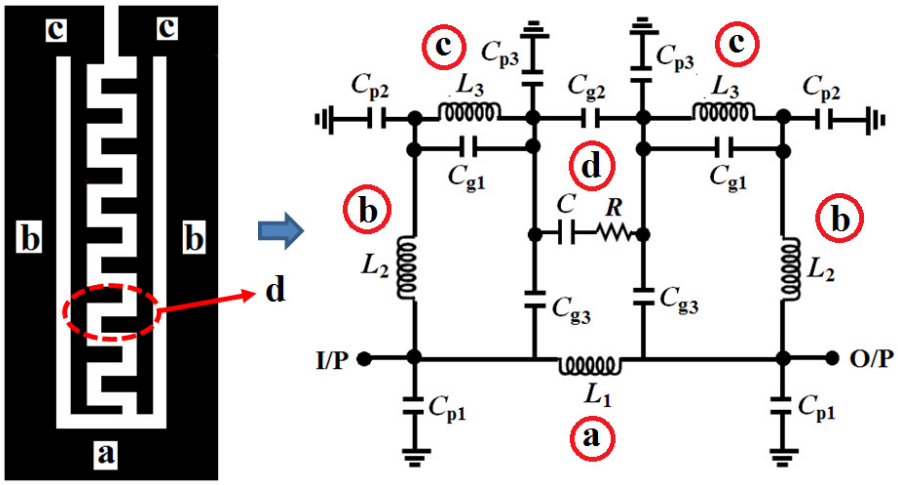

Figure 4. Equivalent circuit diagram of the unit CCDFHL cell in lumped elements.

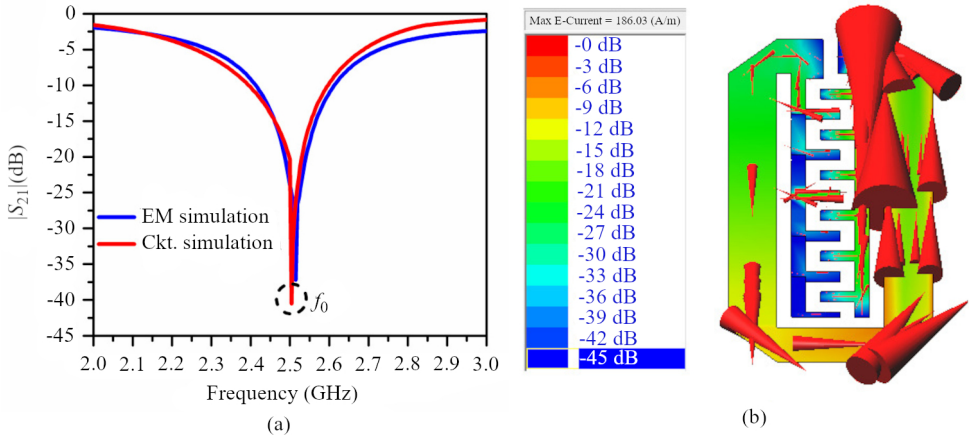

Figure 5. (**a**) Comparison of the EM and circuit simulated $|S_{21}|$ (dB) of the unit CCDFHL cell, (**b**) surface current vectors distribution plot for a CCDFHL cell at f_0 = 2.5 GHz.

3. Resonant characteristics of a pair of CCDFHL cells

Figure 6a depicts the structure of a pair of CCDFHL cells. The hybrid mode is used to cascade the cells. In image Figure 6b, the pair of DFHL and CCDFHL cells' EM simulated $|S_{21}|$ (dB) plots are compared, and the passband response is highlighted in the inset image. Figure 6b shows that the attenuation level in the passband has been reduced more as a result of the centrally corrugated arms pair's effective surface area being smaller. However, the bandwidth of the passband as indicated in the inset diagram has been reduced greatly compared to that for the DFHL cells pair of [22]. The capacitive effects of the IDC cause such phenomenon, justifying the ability to design a narrow bandpass filter by such CCDFHL cells. Furthermore, CCDFHL cells exhibit lower attenuation levels of higher-order harmonics (by 9 dB) compared to DFHL cells, indicating the efficacy of CCDFCL cells in enhancing stopband response. Figure 7a,b shows the distribution of surface currents at the even- and odd-mode resonant frequencies, f_{oe} and f_{oo}.

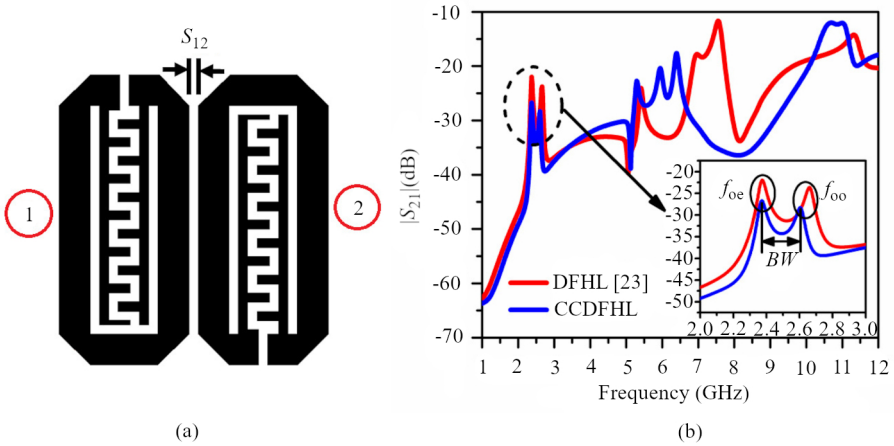

Figure 6. (**a**) Structure of a pair of CCDFHL cells, (**b**) comparison of $|S_{21}|$ (dB) between a pair of DFHL cells [23] and CCDFHL cells (passband response is shown in the inset figure).

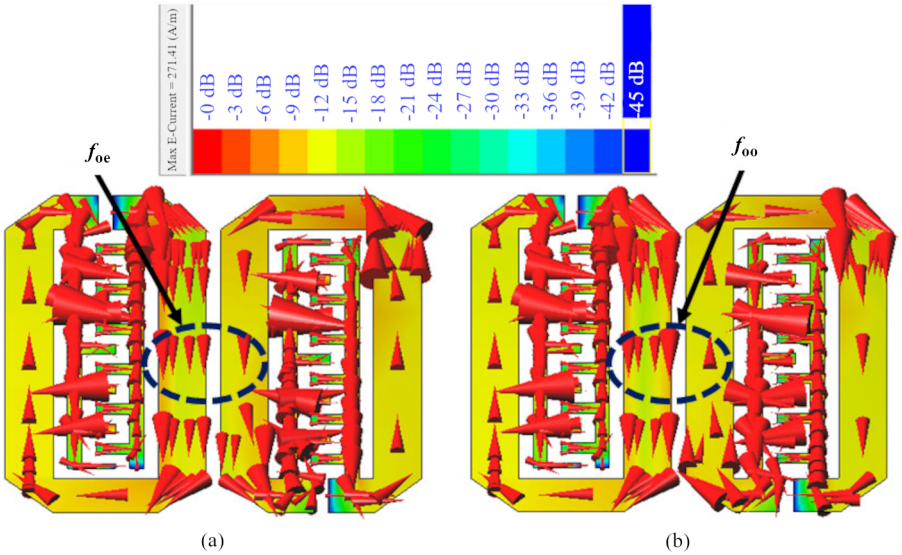

Figure 7. Surface currents of the CCDFHL cells at (**a**) f_{oe} = 2.38 GHz, and (**b**) f_{oo} = 2.61 GHz.

The even-mode (Figure 7a) currents have been observed to be unidirectional, but the odd-mode (Figure 7b) currents have been observed to be in opposition to one another. The imbalance between the phase velocities of such modes is the main cause of harmonic production for a hairpin-line filter [1]. Because of its smaller phase constant, the odd-mode propagates with a higher phase velocity than the even-mode in general. The CCDFHL cells' four sharp corners have been tapered in order to lessen the radiation that results from the sudden changes in the signal directions at the corners. Next, by cascading the CCDFHL cells, a fourth-order bandpass filter (CCDFHLBF) is built in the next section.

4. Design of the fourth-order CCDFHLBF

Four has been determined to be the filter's order based on the criteria given in Table 1 [1]. g_1 = 0.7129, g_2 = 1.2004, g_3 = 1.3213, g_4 = 0.6476, and g_5 = 1.1008 are the elements of the prototype low-pass filter with a passband ripple of 0.01 dB that may be obtained from [1]. The first and fourth cells' external quality factors, as well as the coupling coefficients

between the neighbouring cells, are as follows: $Q_{e1} = Q_{e4} = 23.76$, $M_{1,2} = M_{3,4} = 0.0324$, $M_{2,3} = 0.0238$. Figure 8 shows how the coupling coefficient varies in relation to the coupling gap between the two CCDFHL cells. It has been discovered that the coupling gaps S_{ij} (Figure 8) have starting values of 0.9 mm and 1.18 mm. As a result, Figure 9 shows the optimised dimensions of the filter based on fourth-order CCDFHL cells. The filter measures 281.73 mm^2, or $0.44\lambda_g \times 0.14\lambda_g$. A 14.2% reduction in size has been achieved in comparison to that reported in [23]. Figure 10 explores the simulated *S*-parameters of the CCDFHLBF. It has been discovered that the passband response has become excellent and the skirt properties have significantly improved. There was an insertion loss of 1.2 dB and a return loss of 16 dB. Its use for multichannel receivers is limited, nonetheless, by the unsatisfactory attenuation levels at spurious harmonics (more than 10 dB).

Table 1. Specifications of the filter.

Parameters	Notations	Specifications
Mid-band Frequency	f_0	2.5 GHz
Fractional Bandwidth	*FBW*	3%
3 dB Bandwidth	*BW*	75 MHz
Insertion Loss	*IL*	<3 dB
Passband Ripple	L_{Ar}	0.01 dB
Return Loss	*RL*	>15 dB

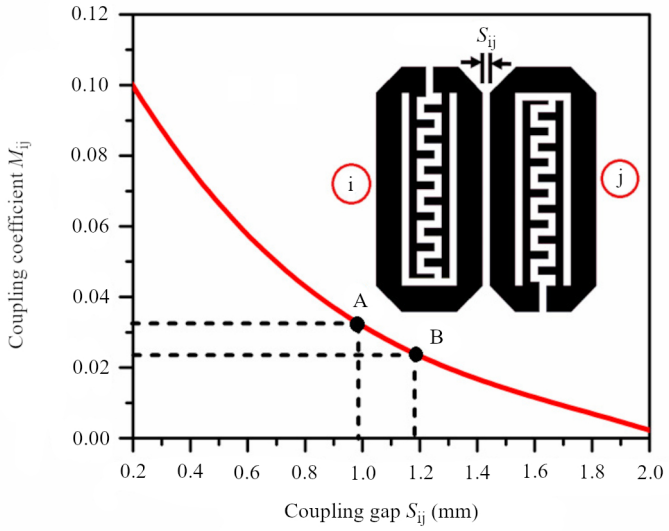

Figure 8. Change in the coupling coefficient M in relation to the coupling gap S (mm) for two CCDFHL cells.

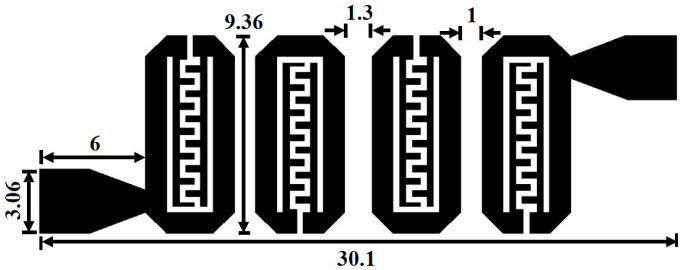

Figure 9. The configuration of the bandpass filter with a center frequency of 2.5 GHz based on fourth-order CCDFHL cells. Every dimension is in mm.

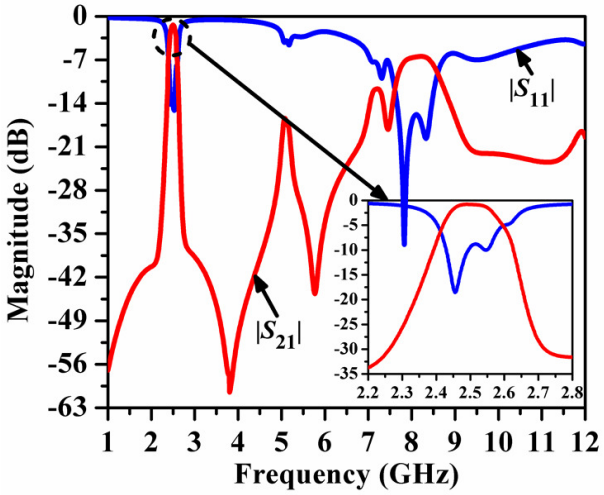

Figure 10. *S*-parameters of the fourth-order bandpass filter, derived from the passband response of CCDFHL cells (inset figure).

Figure 11 shows the equivalent circuit diagram for the bandpass filter based on fourth-order CCDFHL cells. As was previously described, the values of the lumped elements were calculated using traditional transmission line theory.

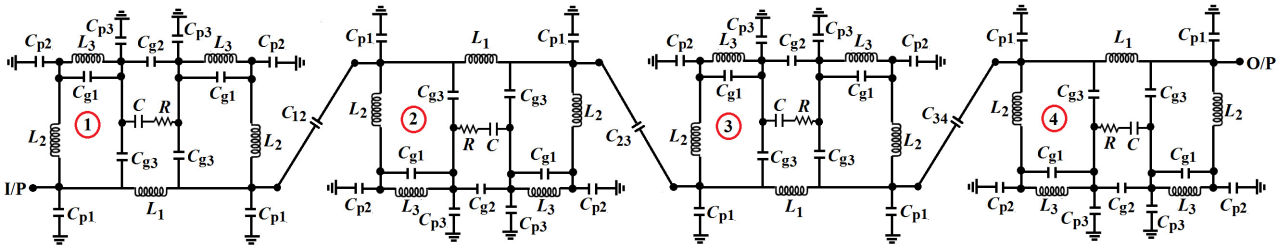

Figure 11. Equivalent circuit diagram of the fourth-order CCDFHL cells based bandpass filter in lumped elements.

The values of the lumped elements have been computed as L_1 = 2.426 nH, L_2 = 3.011 nH, L_3 = 1.169 nH, $C_{p1} = C_{p2}$ = 0.167 pF, C_{p3} = 0.287 pF, $C_{g1} = C_{g2} = C_{g3}$ = 0.015 pF, C_{14} = 0.015 pF, $C_{12} = C_{34}$ = 0.035 pF, C_{23} = 0.238 pF, C = 0.1036 pF, and R = 0.1023 mΩ. The $|S_{21}|$ (dB) curves generated by the EM and circuit simulation, as shown in Figure 12, are in close agreement in both the passband and stopband. However, the locations of the harmonics and the multiple transmission zeros have not matched properly. It happens due to the tolerances arisen from the existence of multiple bends and open ends in the CCDFHL cells which have not been considered in the circuit simulation to avoid complexity. The distribution of the surface currents has been plotted in Figure 13 at the center frequency of 2.5 GHz. It has been revealed that the surface currents have reached at the output port in a large strength due to the passband. Furthermore, the central IDC has become heavily filled with current vectors.

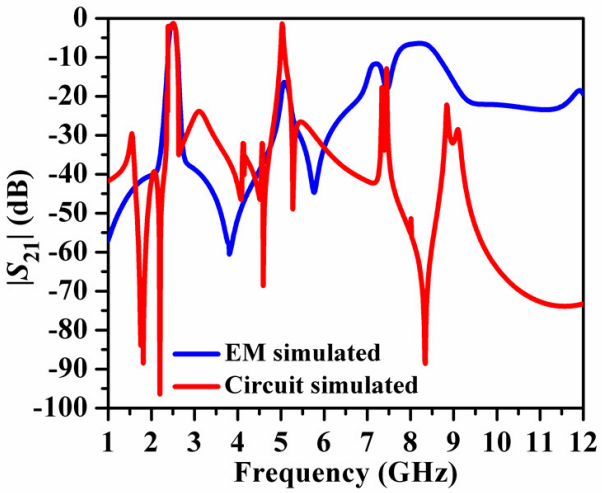

Figure 12. Comparison of the $|S_{21}|$ (dB) curves for the fourth-order bandpass filter created with the CCDFHL cells utilising circuit simulation and electromagnetic modelling.

Figure 13. Surface currents for a fourth-order bandpass filter based on CCDFHL cells at f_0 = 2.5 GHz.

The existence of harmonics with substantial attenuation levels inhibits the implementation of the proposed filter in wireless communications, even though the filter's size has been lowered and the passband responsiveness has improved. As a result, as the next section explains, meander spurline has been integrated with the coupling arms of the nearby CCDFHL cells.

5. Harmonic suppression by meander spurline

A meander spurline, as described in [30], is a modification of the ordinary spurline that produces a zigzag path in the resonator to produce a slow-wave effect for the propagating signal's odd-mode. As a result, the attenuation levels at the harmonics have gradually lowered and the modal phase velocity imbalance has been rectified [24]. Figure 14a illustrates a meander spurline, whereas Figure 14b presents its matching *LCR* model. In Figure 14b, *R* is included to account for conductor loss and radiation impact, and the *LC* resonator is thought to correspond to the spurline slots. The frequency response of $|S_{21}|$ (dB) for a quarter-wavelength line is highlighted in Figure 15.

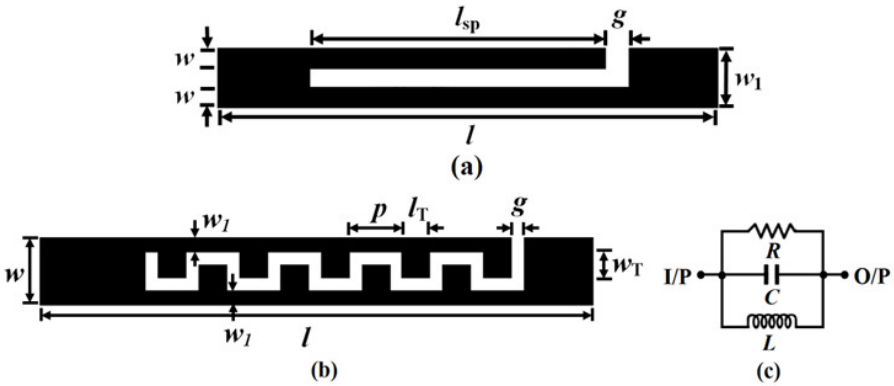

Figure 14. (**a**) Layout of a quarter-wavelength line with a conventional spurline meander spurline, (**b**) layout of a quarter-wavelength line with a meander spurline, (**c**) equivalent circuit diagram.

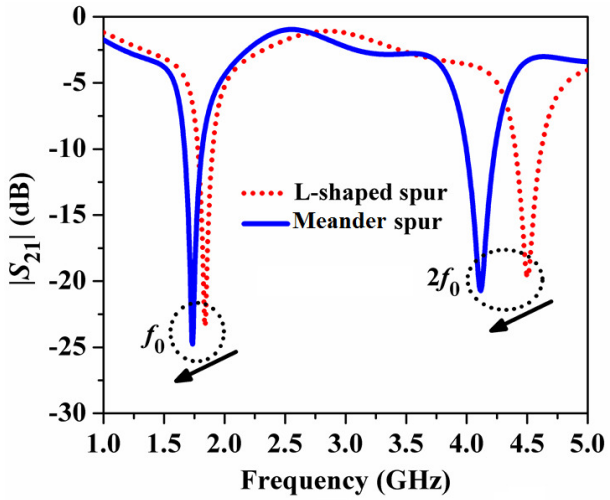

Figure 15. Comparison of $|S_{21}|$ (dB) between the conventional and meander spurline lines. The dimensions are l = 17.07 mm, $l$sp = 13 mm, 17.07 mm, $w = g$ = 0.3 mm, w_1 = 1 mm for the conventional L-shaped spurline, and l = 17.07 mm, w_1 = 0.2 mm, $l_T = w_T$ = 0.8 mm, g = 0.2 mm and w = 1 mm for meander spurline.

Due to the increased slow-wave feature over traditional spurline, it has been noticed that the meander spurline has demonstrated a more narrow and abrupt stopband with the resonance frequency of f_0 = 1.75 GHz (attenuation level of 25 dB) and $2f_0$ = 4.15 GHz (attenuation level of 22 dB). Additionally, the change in f_0 and $2f_0$ to lower frequencies is a result of the line's increased effective electrical length. To tailor the resonance frequency at f_0 = 2.5 GHz, the line's overall length must be shortened. As a result, the meander spurline-based final filter will have a smaller overall size than the traditional spurline-based filter. This demonstrates why the meander spurline is more successful than the traditional spurline and for the same reason the coupled arms of the unit CCDFCL cells have been perturbed by the meander spurline.

5.1 *Study of unit CCDFHL cell with meander spurline*

Consequently, as seen in Figure 16a, a meander spurline of this type has been integrated with the connected arm of the unit CCDFHL cell. Here, l_1 = 9.36 mm, l_2 = 4.2 mm, g = 0.2 mm, and l_{sp} = 6 mm are the expected dimensions. As the number of periodic slots N for the meander spurline increases, the attenuation level at f_0 is gradually increasing while those at $2f_0$ and $3f_0$ are significantly decreasing, according to the wideband frequency responses of the $|S_{21}|$ (dB) curves, as shown in Figure 16b. Additionally, two distinct gearbox zeros have been produced in the stopband, denoted as $2f_z$ and $3f_z$. This phenomenon supports the meander spurline's ability to suppress harmonics. The equivalent circuit diagram

for the unit CCDFHL cell with meander spurline was created by using the same method as was covered in the previous section; it is shown in Figure 17a. The values of L' = 1.53 nH, C' = 1.762 pF, and R' = 4.235 kΩ, in addition to the lumped elements, are the same as those in Figure 4. Figure 17b compares the $|S_{21}|$ (dB) curves simulated by circuit and by EM, and it can be seen that they correspond nicely. However, because there are fewer effective conductive areas in the cell than in the unit CCDFHL cell without meander spurline (Figure 4), the attenuation level at f_0 has increased. The distribution of surface currents as shown in Figure 18a,b at f_0 = 2.23 GHz and $2f_z$ = 5.38 GHz has been used to justify this phenomena. As expected, Figure 18 demonstrates that current vectors have been densely packed at f_0 in relation to $2f_z$. As a result, the investigation has been expanded for two CCDFHL cells in the next section.

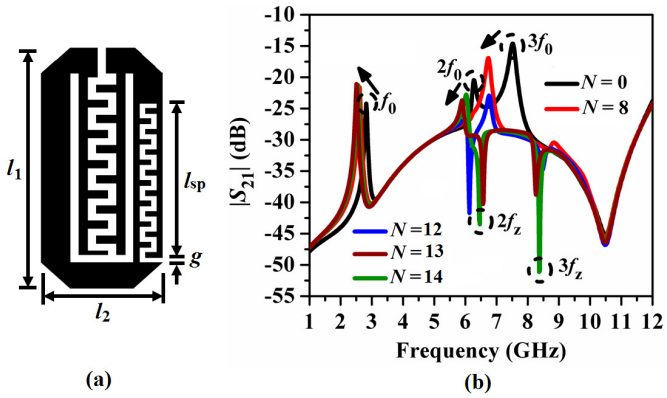

Figure 16. CCDFHL unit cell with meander spurline: (**a**) schematic diagram, (**b**) broad band resonant properties of $|S_{21}|$ (dB).

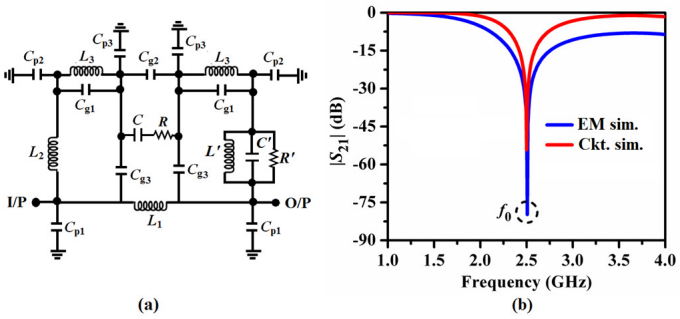

Figure 17. (**a**) Equivalent circuit schematic for the unit CCDFHL cell featuring a meander spurline; (**b**) comparison between the curves for $|S_{21}|$ (dB) generated by circuit simulation and EM.

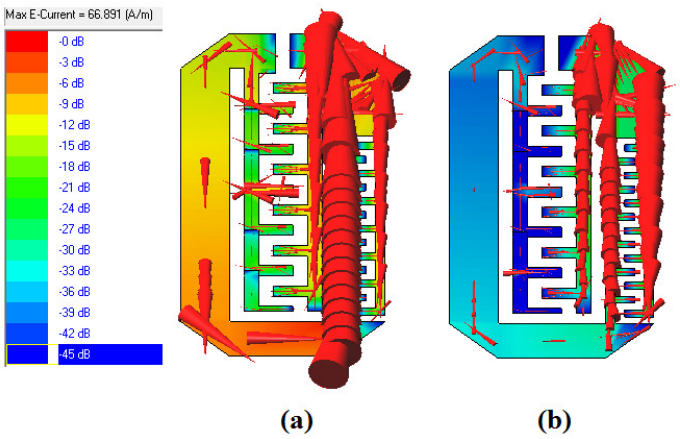

Figure 18. Surface currents for the unit CCDFHL cell with meander spurline at (**a**) f_0 = 2.23 GHz, (**b**) $2f_z$ = 5.38 GHz.

5.2 *Pair of CCDFHL cells with meander spurline*

Figure 19 shows the structure of a pair of CCDFHL cells with meander spurline integrated into the connected arms. Consequently, Figure 20a shows that, subject to an increase in the meander line's number of slots, the two resonant peaks are trending closer to one another, with the odd-mode peak increasing at a faster pace than the even-mode peak. This explains why spurline is used to compensate for the two modes' phase velocities. Furthermore, it can be seen in Figure 20b that three distinct transmission zeros—f_{z1}, f_{z2}, and f_{z3}, have been produced in the stopband, resulting in the suppression of the spurline-induced attenuation levels of the harmonics. In order to comprehend the impact of meander spurline on the even- and odd-mode of the signal, Figure 21a,b presents the surface current distributions for the two CCDFHL cells at frequencies of f_{oe} = 2.17 GHz and f_{oo} = 2.32 GHz, respectively. In the connected zones, it is noticed that, as expected, the directions of the strong currents are opposite for the odd-mode and the same for the even-mode.

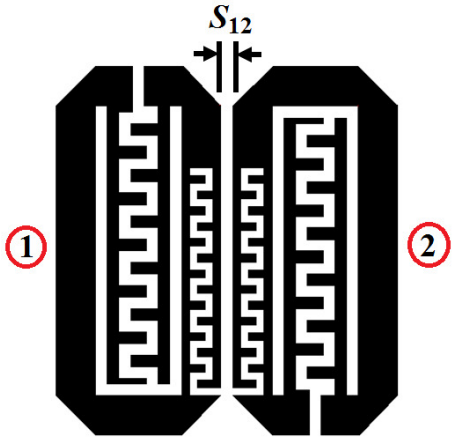

Figure 19. Structure of a pair of CCDFHL cells with meander spurline.

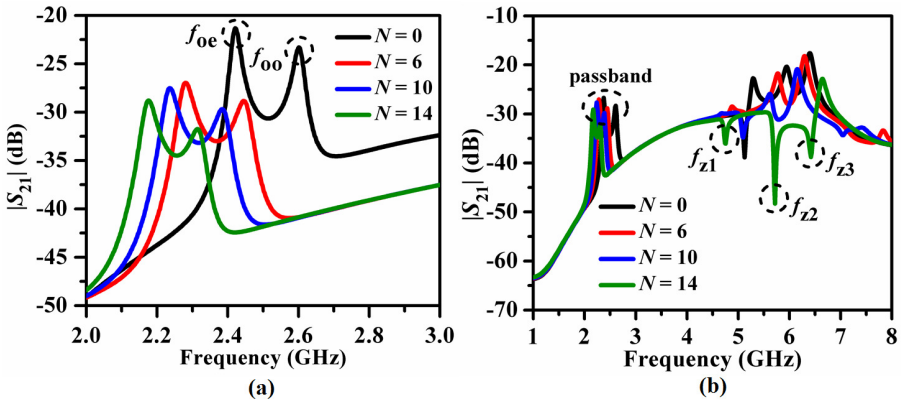

Figure 20. (**a**) Variation of even- and odd-mode resonant frequencies, (**b**) comparison of wideband resonant frequency curves for a pair of CCDFHL cells with different values of *N*.

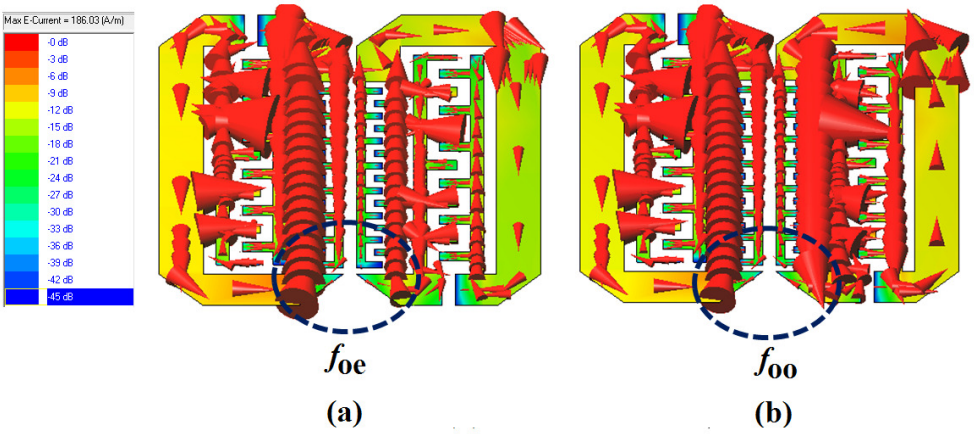

Figure 21. Surface currents for a pair of CCDFHL cells with N = 14 at (**a**) f_{oe} = 2.17 GHz, (**b**) f_{oo} = 2.32 GHz.

6. Fourth-order filter with spurline

Figure 22 illustrates the coupling coefficient M's variation with the coupling gap S (mm) for two meander spurline-based CCDFHL cells. From this, the coupling gap's initial values were determined to be $S_{12} = S_{34} = 0.62$ mm and $S_{23} = 0.94$ mm, which corresponded to the coupling coefficients $M_{1,2} = M_{3,4} = 0.0324$ and $M_{2,3} = 0.0238$. Consequently, Figure 23 displays the optimised size of the fourth-order CCDFHL cells based filter with spurline. The filter's size is 233.67 mm^2, or $0.43\lambda_g \times 0.12\lambda_g$, which results in a 24% reduction in size [23].

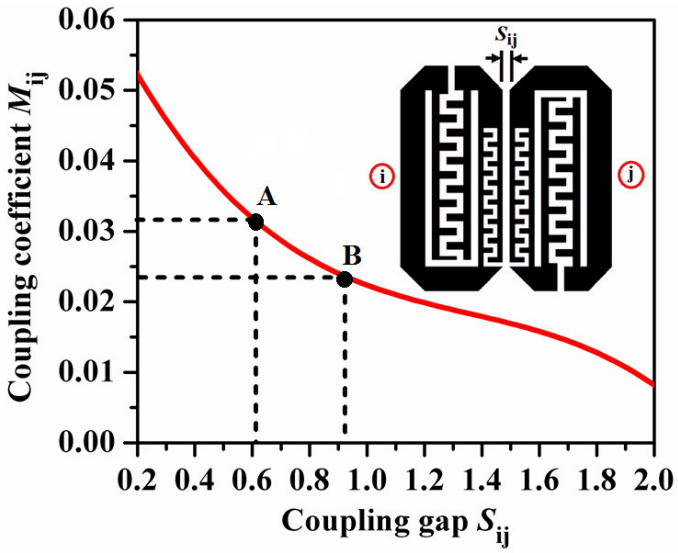

Figure 22. Variation of a pair of CCDFHL cells with spurline in the coupling coefficient M vs. coupling gap S (mm).

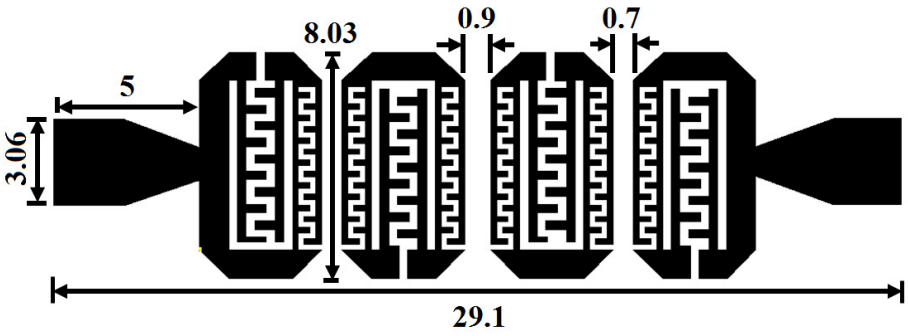

Figure 23. The configuration of the bandpass filter with a center frequency of 2.5 GHz, based on fourth-order CCDFHL cells. Every measurement is in millimetres.

Figure 24a examines the comparison of the simulated *S*-parameters for the CCDFHLBF for the scenarios with and without spurline. It is noted that the filter's skirt characteristic has much improved, and the passband response now exhibits a satisfactory insertion loss of 1.1 dB and return loss of 26 dB. Up to $3.76f_0$, a broad stopband with an attenuation level of less than 38 dB was attained. Furthermore, several transmission zeros have been produced in the passband, enhancing the filter's ability to suppress harmonics. The improvement of the performances of the proposed rectangular corrugated CCDFHL cells based fourth-order filter over that based on trapezoidal corrugated CCDHHL cells has been explored in Figure 24b. It has been revealed that the stopband rejection level of 35 dB of $|S_{21}|$ curve has been obtained in simulation up to $4.8f_0$ compared to 28 dB for that of the filter proposed in [25]. It clearly justifies the effectiveness of the proposed rectangular corrugated CCDFHL cells over the trapezoidal corrugated cells in [25] with respect to the harmonics suppression performance. Subsequently, the equivalent circuit of the fourth-order CCDFHL cells based bandpass filter with spurline has been depicted in Figure 25, in which the values of the lumped elements have been computed as L_1 = 2.316 nH, L_2 = 3.025 nH, L_3 = 1.143 nH, $C_{p1} = C_{p2}$ = 0.143 pF, C_{p3} = 0.267 pF, $C_{g1} = C_{g2} = C_{g3}$ = 0.015 pF, C_{14} = 0.015 pF, $C_{12} = C_{34}$ = 0.031 pF, C_{23} = 0.228 pF, C = 0.104 pF, and R = 0.1023 mΩ, L' = 1.33 nH, C' = 1.562 pF and R' = 4.115 kΩ. It has been found that the $|S_{21}|$ (dB) curves produced by EM- and circuit-simulations, as illustrated in Figure 26, are in good agreement in the passband.

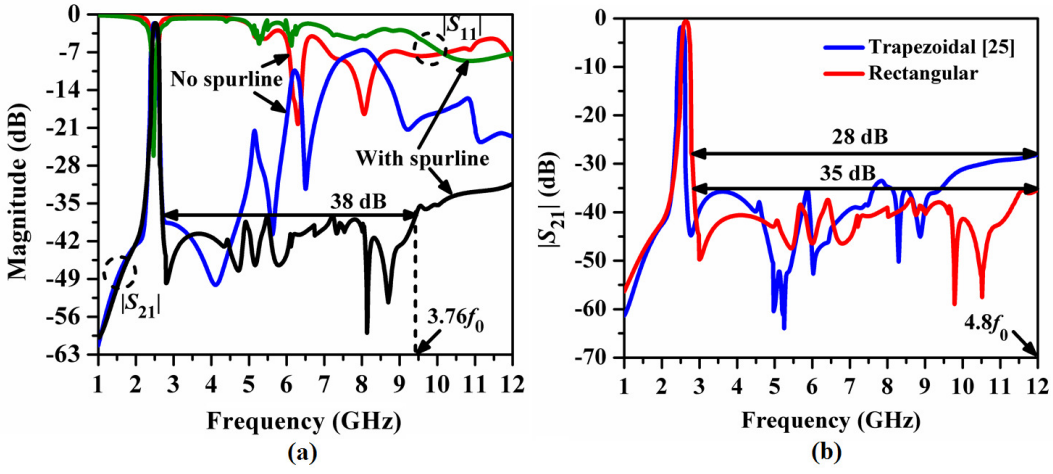

Figure 24. (**a**) Comparison of *S*-parameters curves for the fourth-order bandpass filters based on CCDFHL cells for the cases without and with spurline, (**b**) comparison of $|S_{21}|$ (dB) curves for the fourth-order bandpass filters based on trapezoidal [25] and rectangular CCDFHL cells with spurline.

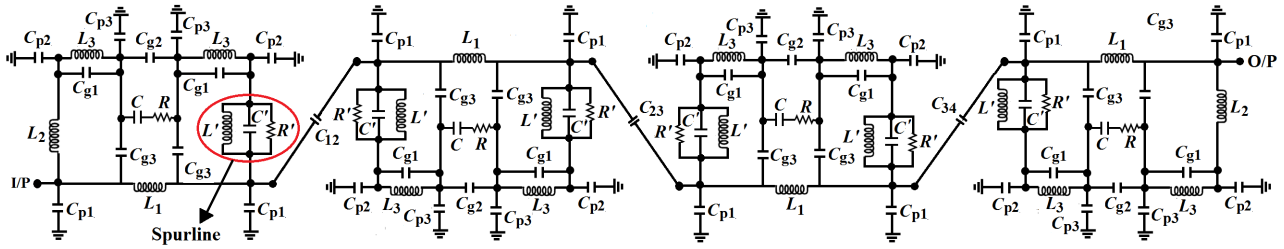

Figure 25. Equivalent circuit of the fourth-order CCDFHL cells based bandpass filter with meander spurline in lumped elements.

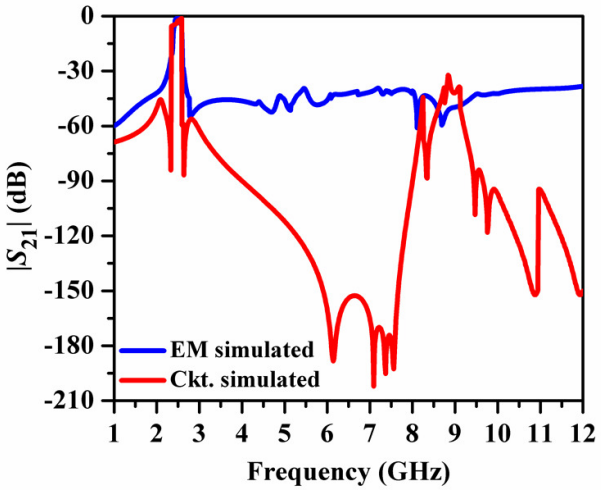

Figure 26. Comparison of the EM- and circuit-simulated $|S_{21}|$ (dB) curves for the fourth-order bandpass filter designed using meander spurline based CCDFHL cells.

A wide stopband with rejection level below 35 dB has been obtained in circuit simulation. In addition, four transmission zeros have been generated in the stopband from 6 GHz to 8 GHz with attenuation level more than 180 dB, justifying the effective conversion of lumped elements from the microstrip lines. The reason for the mismatches for some portions is due to the fact that the ground plane in EM simulation has been considered with infinite dimension, whereas finite ground plane has been considered for circuit simulation. Moreover, the fringing field effects and parasitic effects due to sharp bend edges of the microstrip cell structure have been ignored to avoid the complexity of the circuit model. Figure 27 compares the variation of group delay of S_{21} for the fourth-order bandpass filter with and without meander spurline. It has been revealed that a minimum value of 10 ns is maintained in the passband from 2.45 GHz to 2.55 GHz as expected. Two sharp spikes have been observed with values of 43 s at 2.37 GHz and 45 s at 2.63 GHz for the filter with meander spurline. Such phenomenon indicates the improvement of the skirt characteristics due to the spurline.

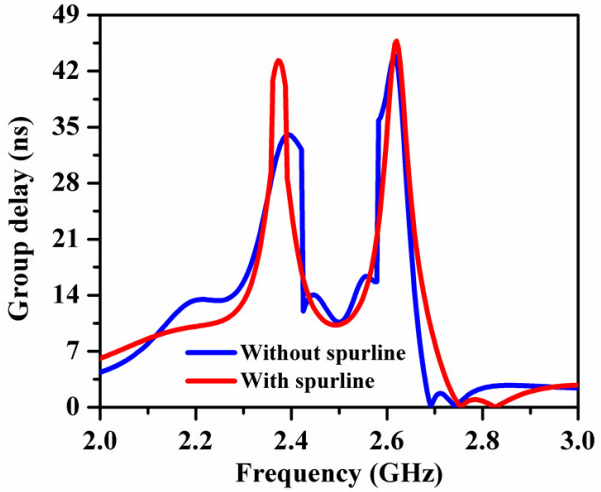

Figure 27. Comparison of the EM simulated group delay (ns) plots of S_{21} for the fourth-order bandpass filter with and without spurline.

7. Experimental results and analysis

As seen in Figure 28a,b, two prototypes of the suggested filters—one with and one without a spurline—have been constructed. The VNA used for the experiment, model number N9928A from Keysight Technologies, has been constructed. Figure 29a,b compare the EM simulated and measured *S*-parameters for the fourth-order CCDFHL filter without spurline (Figure 28a). It has been seen that the curves in the passband and stopband nearly match one another. Measured return loss was 25 dB, and measured insertion loss was 1.3 dB. The harmonics are attenuated to a level greater than 8 dB. The EM simulated and measured *S*-parameters for the filter with spurline (Figure 28b) are then compared in Figure 30a,b. The measurement yielded a wide stopband with an attenuation level of 42 dB up to $4.36f_0$ and a passband insertion loss of 1.1 dB. The filter with a spurline has been shown to suppress the attenuation level at the harmonics by 35 dB when compared to the filter without a spurline. Moreover, the creation of transmission zeros at the passband's boundaries has significantly enhanced the skirt characteristic. Furthermore, there have been several transmission zeros produced in the stopband, which supports the meander spurline's improved ability to suppress harmonics.

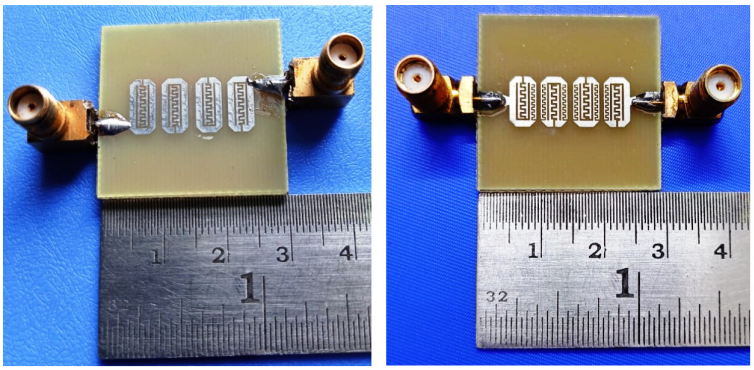

Figure 28. Fourth-order bandpass filter prototypes that were fabricated using CCDFHL cells—(**a**) without a spurline and (**b**) with one.

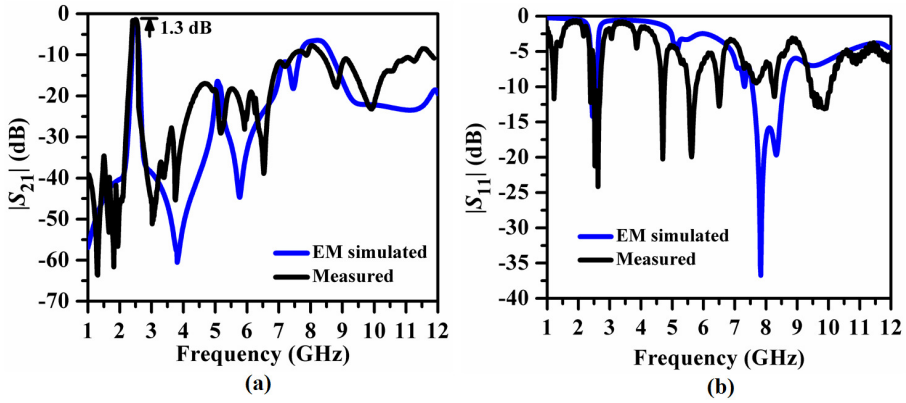

Figure 29. Comparison of the EM simulated and measured *S*-parameters curves for the fourth-order CCDFHL filter without spurline: (**a**) $|S_{21}|$ (dB), and (**b**) $|S_{11}|$ (dB).

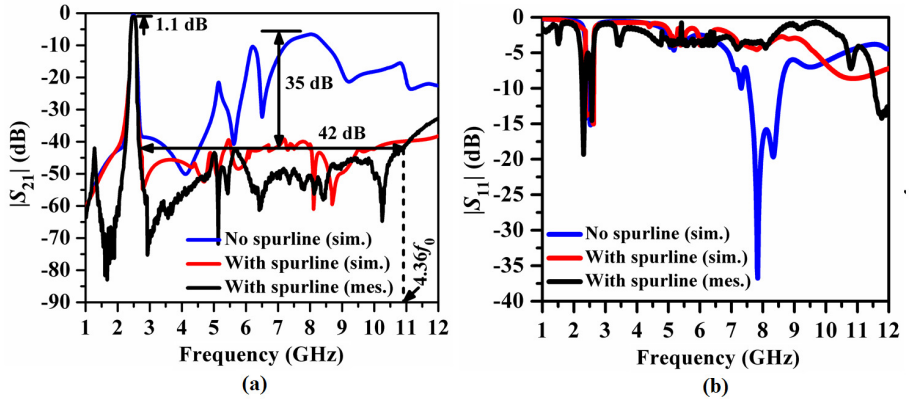

Figure 30. Comparison of the EM simulated and measured *S*-parameters curves for the fourth-order CCDFHL filter for the cases with and without spurline: (**a**) $|S_{21}|$ (dB), and (**b**) $|S_{11}|$ (dB).

As seen in Figure 30b, the return loss in the passband has been found to be greater than 15 dB. Thus, at f_0 and $2f_0$, the surface current distributions have been investigated in Figure 31a,b. Figure 31a shows how strongly the currents have propagated through the filter's structure for the passband, but Figure 31b shows how weakly they have done so for the stopband. The filters are generally characterized by the following parameters [31]:

- the roll-off rate ξ (dB/GHz) generally used to measure skirt selectivity defined as:

$$\xi = \frac{\alpha_s - \alpha_c}{f_s - f_c} \tag{5}$$

where α_s is the 25 dB attenuation point and α_c is the 3 dB attenuation point; f_s is the 30 dB stopband frequency and f_c is the 3 dB cutoff frequency.

- The relative stopband frequency f_{SB} defined as:

$$RSB = \frac{f_{SBW}}{f_{SC}} \tag{6}$$

where f_{SBW} is the 25 dB stopband bandwidth and f_{SC} is the stopband center frequency.

- The suppression factor *SF* is the parameter that indicates the degree of stopband suppression. It is defined as:

$$SF = \frac{SBRL}{10} \tag{7}$$

where *SBRL* is the stopband rejection level of consideration.

- The normalized circuit size *NCS* indicates the degree of miniaturization of the filters and it is defined as:

$$NCS = \frac{physical\ size\ \ (length \times width)}{\lambda_g \times \lambda_g} \tag{8}$$

- Finally, the figure-of-merit (*FOM*) is the overall performance index of the proposed filters, and it is defined as:

$$FOM = \frac{\xi \times RSB \times SF}{NCS \times AF} \tag{9}$$

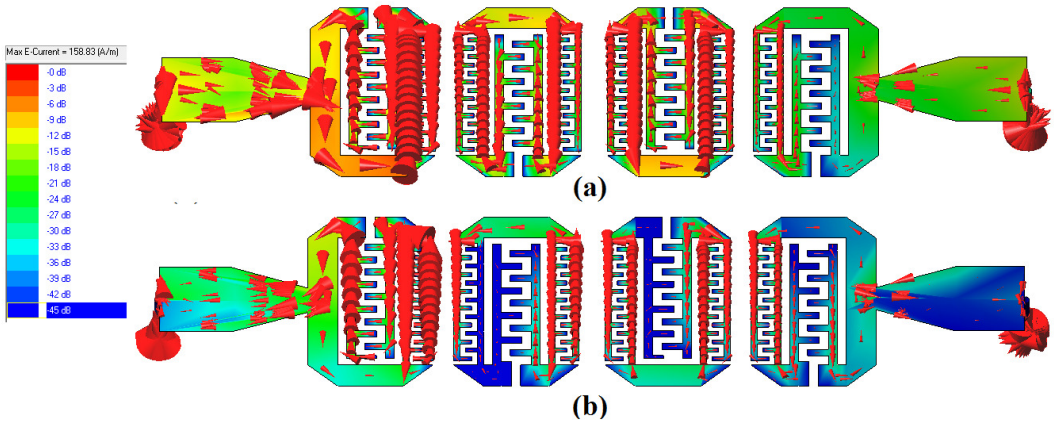

Figure 31. Surface currents for the fourth-order bandpass filter with spurline based CCDFHL cells (**a**) f_0 = 2.5 GHz, (**b**) $2f_0$ = 5.0 GHz.

From Table 2, it is found that the proposed design has occupied less circuit area than those in [16, 19, 20, 21, 22, 23, 24]. It has exhibited a higher stopband rejection level than all the filters, achieving a wider stopband bandwidth than the structures proposed in [17, 20, 23, 24, 25]. Moreover, the proposed filter provides maximum value of figure-of-merit (*FOM*). Such comparison justifies the effectiveness of the proposed design compared to other related works. The full form of the comparative parameters in Table 2 are *FBW* = fractional bandwidth, *IL* = insertion loss, *RL* = return loss, *SRL* = stopband rejection level, *SBW* = stopband bandwidth and λ_g = guided wavelength at the center frequency f_0.

Table 2. Comparative study with similar works.

Designs	f_0 (GHz)	FBW (%)	IL (dB)	RL (dB)	SRL (dB)	SBW ($\times f_0$)	Size (λ_g^2)	FOM
This work	2.5	3	1.1	15	42	4.36	0.0516	14,220.5
[16]	2.8	23	0.2	26	16	5.00	0.1133	587.92
[17]	9.3	9.25	1.58	17.7	18	2.31	0.0053	4470.6
[19]	2.4	15	0.8	20	20.5	8.33	0.9234	1207.1
[20]	10.81	44.5	0.6	22	20	4.00	0.1200	438.84
[21]	2.35	3	0.15	22	21.9	5.64	0.1318	9283.52
[22]	2.5	4	1.6	17	38	4.48	0.0744	8277.03
[23]	2.5	5	2.9	17	39	3.20	0.0539	6669.7
[24]	2.5	4	1.8	16	40	4.00	0.0833	3991.1
[25]	2.5	5	1.45	19	39	3.20	0.0539	5689.5

8. Conclusions

The design of a small fourth-order centrally corrugated hairpin line bandpass filter featuring a meander spurline has been shown in this study. Initially, the traditional hairpin-line filter's open-end arms were modified with rectangular corrugations (IDC) and folded symmetrically inward. As a result, the filter's overall circuit size is 68% smaller than that of a traditional hairpin line filter with the same characteristics. Nonetheless, the centre corrugations have not had a significant

impact on the attenuation levels at the harmonics. In order to accomplish modal phase velocity adjustment, the meander spurlines have subsequently been integrated into the coupled arms of the nearby CCDFHL cells. To achieve the maximum suppression of harmonics, the spurline's size and slot count have been optimally tuned. As a result, the measurement produced an expanded stopband with a rejection level of 42 dB up to $4.36f_0$. Furthermore, compared to the traditional filter without a spurline, a size reduction of 81% was accomplished. For the suggested filter, an appealing figure-of-merit (*FOM*) value of 14,220.5 has been found. The WLAN systems can be designed using the suggested filter.

Conflict of interest

There is no conflict of interest for this study.

References

[1] J. S. Hong and M. J. Lancaster, "Lowpass and Bandpass Filters," in *Microstrip Filter for RF/Microwave Applications*, K. Chang, Ed., 1st ed., New York, NY, USA: John Wiley & Sons, Inc., 2001, pp. 29–76.

[2] K. Kavitha and M. Jayakumar, "Design and performance analysis of hairpin bandpass filter for satellite applications," *Procedia Comput. Sci.*, vol. 143, pp. 886–891, 2018, https://doi.org/10.1016/j.procs.2018.10.366.

[3] A. O. Nwajana, "Circuit Modelling of Bandpass/Channel Filter with Microstrip Implementation," *Indones. J. Electr. Eng. Inform.*, vol. 8, pp. 696–705, 2020, https://doi.org/10.11591/ijeei.v8i4.2466.

[4] K. S. Saleh, W. Ismail, I. S. Abidin, M. H. Jamaluddin, M. H. Bataineh, and A. S. Alzoubi, "5G hairpin bandpass filter," *Jordan. J. Comput. Inf. Technol.*, vol. 7, pp. 1–12, 2021, https://doi.org/10.1186/s12889-021-10758-0.

[5] A. Zakharov, S. Rozenko, S. Litvintsev, and M. Ilchenko, "Hairpin Resonators in Varactor-Tuned Microstrip Bandpass Filters," *IEEE Trans. Circuits Syst. II Express Briefs*, vol. 67, pp. 1874–1878, 2013, https://doi.org/10.1109/TCSII.2019.2953247.

[6] A. S. Kim and N. Y. Kim, "Compact bandpass filter with wide stop band response based on meandered-line stepped-impedance resonator using IPD process," *Microw. Opt. Technol. Lett.*, vol. 57, pp. 1466–1470, 2015, https://doi.org/10.1002/mop.29111.

[7] Z. Troudi, J. Machac, and L. Osman, "Miniaturized planar band-pass filter based on interdigital Arm SRR," *IET Microw. Antennas Propag.*, vol. 13, pp. 2081–2086, 2019, https://doi.org/10.1049/iet-map.2018.5708.

[8] E. S. Kim, K. K. Adhikari, and N. Y. Kim, "Miniaturized high-selectivity microstrip bandpass filter using capacitively coupled stub-loaded stepped-impedance resonators," *Microw. Opt. Technol. Lett.*, vol. 58, pp. 2004–2010, 2016, https://doi.org/10.1002/mop.29958.

[9] Y. S. Mezaal and A. S. Al-Zayed, "Design of microstrip bandpass filters based on stair-step patch resonator," *Int. J. Electron.*, vol. 106, pp. 477–490, 2019, https://doi.org/10.1080/00207217.2018.1545144.

[10] G. M. Aristarkhov, A. Grebennikov, and N. V. Zvezdinov, "High-Selectivity Microstrip Filters Based on Structures With a Limited Number of Hairpin Resonators [Application Notes]," *IEEE Microw. Mag.*, vol. 20, pp. 22–31, 2019, https://doi.org/10.1109/MMM.2019.2935362.

[11] F. Wang, L. Ke, X. Yin, N. Yu, and Y. Yang, "Compact TSV-based hairpin bandpass filter for THz applications," *IEEE Access*, vol. 9, pp. 132078–132083, 2021, https://doi.org/10.1109/ACCESS.2021.3107537.

[12] C. Luo, et al., "Quasi-reflectionless microstrip bandpass filters using bandstop filter for out-of-band improvement," *IEEE Trans. Circuits Syst. II Express Briefs*, vol. 67, pp. 1849–1853, 2019, https://doi.org/10.1109/TCSII.2019.2946915.

[13] K. L. Du and M. N. S. Swamy, "RF and microwave subsystems," in *Wireless Communication Systems: From RF Subsystems to 4G Enabling Technologies*, Cambridge, UK: Cambridge University Press, 2010, pp. 373–463.

[14] H. P. Partal, "Cross coupled wiggly line hairpin filters with high selectivity and spurious suppression," in *Proc. 40th Eur. Microw. Conf.*, Paris, France, 2010, https://doi.org/10.23919/EUMC.2010.5616289.

[15] A. A. Lotfi-Neyestanak and A. Lalbakhsh, "Improved microstrip hairpin-line bandpass filters for spurious response suppression," *Electron. Lett.*, vol. 48, pp. 858–859, 2012, https://doi.org/10.1049/el.2012.0967.

[16] J. Marimuthu, K. S. Bialkowski, and A. Abbosh, "Compact bandpass filter with sharp passband and wide harmonic suppression using miniaturized coupled structure loaded with stepped-impedance stubs," *Microw. Opt. Technol. Lett.*, vol. 58, pp. 2505–2508, 2016, https://doi.org/10.1002/mop.30089.

[17] S. N. Dembele, T. Zhang, J. Bao, and D. Bukuru, "Compact microstrip bandpass filter using dual closed-loop stepped impedance resonator," *Int. J. Microw. Wireless Technol.*, vol. 10, pp. 405–411, 2018, https://doi.org/10.1017/S1759078718000405.

[18] F. Cheng, P. Lu, and K. Huang, "Realization of transmission zeros for bandpass filter using inductive-coupled stub-loaded resonators," *Int. J. Microw. Wireless Technol.*, vol. 12, pp. 34–38, 2019, https://doi.org/10.1017/S1759078719001041.

[19] C. W. Tang, C. H. Teng, and J. M. Sun, "Design of wide-stopband microstrip bandpass filter with assistance of spur lines," *Electron. Lett.*, vol. 49, pp. 126–127, 2013, https://doi.org/10.1049/el.2012.3384.

[20] T. Huang, Z. H. Shao, and Z. Chen, "Miniaturized wideband bandpass filter with enhanced selectivity and stopband suppression," *Microw. Opt. Technol. Lett.*, vol. 60, pp. 769–772, 2018, https://doi.org/10.1002/mop.31052.

[21] H. Liu, et al., "Wide-stopband superconducting bandpass filter using slitted stepped-impedance resonator and composite spurline structure," *IEEE Trans. Appl. Supercond.*, vol. 28, pp. 1–8, 2018, https://doi.org/10.1109/TASC.2018.2858757.

[22] T. K. Das and S. Chatterjee, "Spurline-embedded compact hairpin-line bandpass filters for wide harmonic suppression," *Int. J. Microw. Wireless Technol.*, vol. 14, pp. 553–565, 2021, https://doi.org/10.1017/S1759078721001197.

[23] T. K. Das and S. Chatterjee, "Harmonic suppression by using T-shaped spur-line in a compact hairpin-line bandpass filter," *Radioengineering*, vol. 30, pp. 296–303, 2021, https://doi.org/10.13164/re.2021.0296.

[24] T. K. Das and S. Chatterjee, "Multi-spurious harmonics suppression in folded hairpin line bandpass filter by meander spur-line," *Int. J. RF Microw. Comput. Aided Eng.*, vol. 31, pp. e22858/1–16, 2021, https://doi.org/10.1002/mmce.22858.

[25] T. K. Das and S. Chatterjee, "Wide Stopband Centrally Corrugated Folded Bandpass Filter with Trapezoidal Spurline," in *Proc. IEEE Wireless Antenna Microw. Symp. (WAMS)*, Rourkela, India, 2022, https://doi.org/10.1109/WAMS54719.2022.9848230.

[26] G. Karimi, M. Amirian, A. Lalbakhsh, and M. Ranjbar, "A new microstrip coupling system for realization of a differential dual-band bandpass filter," *AEU, Int. J. Electron. Commun.*, vol. 99, pp. 186–192, 2018, https://doi.org/10.1016/j.aeue.2018.11.004.

[27] A. Lalbakhsh, M. U. Afzal, K. P. Esselle, and S. L. Smith, "All-metal wideband frequency-selective surface bandpass filter for TE and TM polarizations," *IEEE Trans. Antennas Propag.*, vol. 70, pp. 2790–2800, 2022, https://doi.org/10.1109/TAP.2021.3138256.

[28] M. Sharifi and V. Mashayekhi, "Design of a modified hairpin bandpass filter using embedded radial stubs featuring ultrawide stopband," *AEU, Int. J. Electron. Commun.*, vol. 164, pp. 1–9, 2023, https://doi.org/10.1016/j.aeue.2023.154624.

[29] G. D. Alley, "Interdigital capacitors and their application to lumped-element microwave integrated circuits," *IEEE Trans. Microw. Theory Techn.*, vol. MTT-18, pp. 1028–1033, 1970, https://doi.org/10.1109/TMTT.1970.1127407.

[30] C. Nguyen, C. Hsieh, and D. W. Ball, "Millimeter wave printed circuit spurline filters," in *Proc. IEEE MTT-S Int. Microw. Symp. Dig.*, Boston, MA, USA, 1983, pp. 98–100, https://doi.org/10.1109/MWSYM.1983.1130821.

[31] M. Hayati, S. Majidifar, and S. N. Sobhani, "Using a hybrid encoding method based on the hexagonal resonators to increase the coding capacity of chipless RFID tags," *Int. J. RF Microw. Comput. Aided Eng.*, vol. 32, pp. e23474/1–18, 2022, https://doi.org/10.1002/mmce.23474.